# Edge states and ballistic transport in zigzag graphene ribbons: The role of SiC polytypes

A. L. Miettinen,[1] M. S. Nevius,[1] W. Ko,[2] M. Kolmer,[2] A.-P. Li,[2] M. N. Nair,[3] B. Kierren,[4] L. Moreau,[4]
E. H. Conrad,[1,*] and A. Tejeda[5,3]

[1]*The Georgia Institute of Technology, Atlanta, Georgia 30332-0430, USA*
[2]*Center for Nanophase Materials Sciences, Oak Ridge National Laboratory, Oak Ridge, Tennessee 37831, USA*
[3]*Synchrotron SOLEIL, L'Orme des Merisiers, Saint-Aubin, 91192 Gif sur Yvette, France*
[4]*Institut Jean Lamour, CNRS-Université de Lorraine, 54506 Vandoeuvre les Nancy, France*
[5]*Laboratoire de Physique des Solides, Université Paris-Sud, CNRS, UMR 8502, F-91405 Orsay Cedex, France*

Zigzag-edge graphene sidewall ribbons grown on $6H$-SiC $\{11\bar{2}n\}$ facet walls are ballistic conductors. It is assumed that graphene sidewall ribbons grown on $4H$-SiC $\{11\bar{2}n\}$ facets would also be ballistic. In this work, we show that SiC polytype indeed matters: ballistic sidewall graphene ribbons only grow on $6H$-SiC facets. $4H$ and $4H$-passivated sidewall graphene ribbons are diffusive conductors. Detailed photoemission and microscopy studies show that $6H$-SiC sidewall zigzag ribbons are metallic with a pair of $n$-doped edge states associated with asymmetric edge terminations. In contrast, $4H$-SiC zigzag ribbons are strongly bonded to the SiC, severely distorting the ribbon's $\pi$ bands. $H_2$ passivation of the $4H$ ribbons returns them to a metallic state but they show no evidence of edge states in their photoemission-derived band structure.

## I. INTRODUCTION

Epitaxial graphene (EG) is graphene grown from silicon carbide (SiC) [1]. When grown on the SiC(0001) (Si face), it has a known orientation relative to the SiC substrate and can be grown as uniform single layers. The bottom-up growth of EG ribbons on facets of patterned SiC(0001) shallow trenches (known as "sidewall" graphene) was proposed as a viable route towards graphene electronics [1,2], circumventing patterned exfoliated graphene's lithographic limits on ribbon width and edge disorder [3–8]. This is because the edges of EG ribbons are defined entirely by the orientation of the SiC(0001) pregrowth trenches. Trenches parallel to the SiC $\langle1\bar{1}00\rangle$ direction produce zigzag (ZZ) edge ribbons on the SiC step facets (see Fig. 1). Armchair (AC) edge ribbons grow on steps parallel to the SiC $\langle11\bar{2}0\rangle$ direction.

An exciting work found that ZZ-edge sidewall ribbons grown on $6H$-SiC substrates were room temperature ballistic conductors using 2- and 4-point measurements [9,10]. The current development of ballistic devices on modern $4H$ substrates has implicitly assumed that ZZ-edge graphene grown on $4H$- and $6H$-SiC would be the same. However, attempts to measure the band structure of $4H$ ZZ-edge sidewall graphene found no evidence of metallic graphene on the sidewall despite exploring growth conditions up to the melting point of the SiC trenches [11]. Thin metallic graphene strips were found on the (0001) surface near the step edges of the facet, just not on the sidewalls [12]. These conflicting results led to an unresolved question: what structural or growth variables affect ZZ-edge sidewall graphene formation? In this work, we show that the dominant factor in

ZZ-edge sidewall graphene growth is the SiC polytype, not the growth method. Angle-resolved photoemission spectroscopy (ARPES) measurements show that sidewall ZZ ribbons with metallic $\pi$ bands readily grow on $6H$-SiC but not on $4H$-SiC. On $4H$-SiC, the graphene's $\pi$ bands are severely distorted by graphene-Si bonds to the SiC facets, similarly to the graphene-substrate bonding that makes the first graphene layer on SiC(0001) semiconducting [13–16]. $H_2$ passivation of $4H$ ribbons restores the $\pi$ band's metallic character. The $6H$ ZZ-edge ribbons have two flat bands below the Fermi energy ($E_F$). These bands are consistent with the nearly flat edge states predicted for ZZ ribbons with asymmetric edge terminations [17]. The broken symmetry of the $6H$-edge states has the potential to be used in spin valve devices [17]. $4H$-passivated ribbons show no evidence of $n$-doped edge states or a significant band gap. Two-point resistance measurements on $6H$ sidewall ZZ ribbons are independent of the ribbon length, consistent with ballistic transport, while both $4H$ and passivated $4H$ ribbons' resistances are strong functions of the ribbon length, consistent with diffusive conductance.

Figure 2(a) shows 2-point resistance ($R_{2p}$) measurements on different sidewall ZZ ribbons. The figure shows that $R_{2p}$ for $6H$ ribbons is independent of probe separation with a value of $R_{2p} \sim h/e^2$; i.e., they are ballistic conductors like previously measured $6H$ ZZ ribbons [18]. $4H$ and $4H$-passivated ribbons on the other hand show diffusive resistance curves. The resistance of $4H$ and $4H$-passivated ribbons is linear in $L$. Note that Fig. 2(a) is plotted on a log scale so the linear dependence is obscured (see Supplemental Material [20] for details). Similarly, $dI/dV$ measurements of the different sidewall graphene ribbons show that $4H$ ribbons are gapped semiconductors (see Supplemental Material). As we now discuss, the reason for these transport differences is the nature
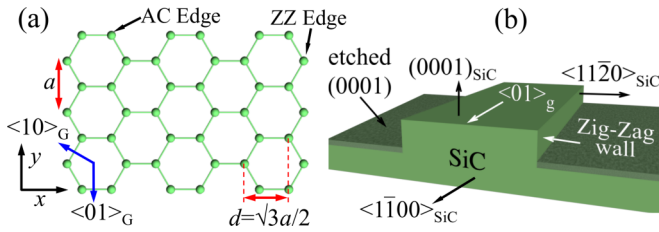
FIG. 1. (a) Graphene lattice. (b) The pregrowth etched SiC(0001) step geometry to grow ZZ-edge sidewall graphene. The distance between ZZ rows is $d = \sqrt{3}a/2$, $a = 2.462$ Å.

of the graphene-substrate interaction on the different SiC polytypes.

## II. EXPERIMENTAL

Samples were prepared starting from a polished SiC(0001) sample from Cree, Inc. Trenches with {11$\bar{2}$0} facet walls are formed by e-beam patterning lines on SiC followed by plasma etching to produce well-defined 25–30 nm deep trenches 400 nm apart over a 1 mm² area. The (0001) trench tops are 200 nm wide. The samples are grown by first using an anneal step to stabilize the step structure [11]. This is followed by a rapid high temperature growth step. The rapid heating grows the graphene quickly thus limiting step melting by preventing Si evaporation through an essentially impervious graphene layer, similarly to carbon-capping methods [19]. Details of the process are found in the Supplemental Material [20] and in Ref. [11]. The ribbons are grown in a confinement-controlled sublimation furnace [21]. The process causes the surface of the step to reorganize into a complicated set of equilibrium facets and simultaneously grow sidewall graphene. Graphene does not grow well on the SiC(0001) plasma-etched trench bottoms [12]. This limits graphene growth to the step walls and a small strip on the (0001) surface at the step edge. To H₂-passivate the post-graphene-growth 4*H*-SiC trenches, samples were heated at 900 °C for 1 hour in an H₂ furnace ($P_{H2} \sim 800$ mtorr). ARPES measurements were done on the high-resolution Cassiopée beamline. The line has a total measured instrument resolution of $\Delta E < 12$ meV using a Scienta R4000 detector with a ±15° acceptance at $\hbar\omega = 36$ eV. Samples were mounted on a 3-axis cryogenic manipulator. The STM experiments were carried out in an ultrahigh-vacuum (UHV) setup with a base pressure in the low $10^{-10}$ mbar range using a commercial low-temperature Omicron microscope that was modified to minimize capacitive coupling (see Supplemental Material [20] and Ref. [22]).

Scanning tunneling spectroscopy (STS) and two-probe transport measurements were made on two different cryogenic four-probe scanning tunneling microscope (4P-STM) systems, one operated at 82 K and the other at 4.6 K [23,24]. All measurements were done under UHV conditions ($< 10^{-10}$ torr). Because the graphene sidewall samples were exposed to the air after growth, they were cleaned prior to measurement by annealing in the UHV chamber at 300–500 °C for a several hours before STM measurements. See Supplemental Material for more details.
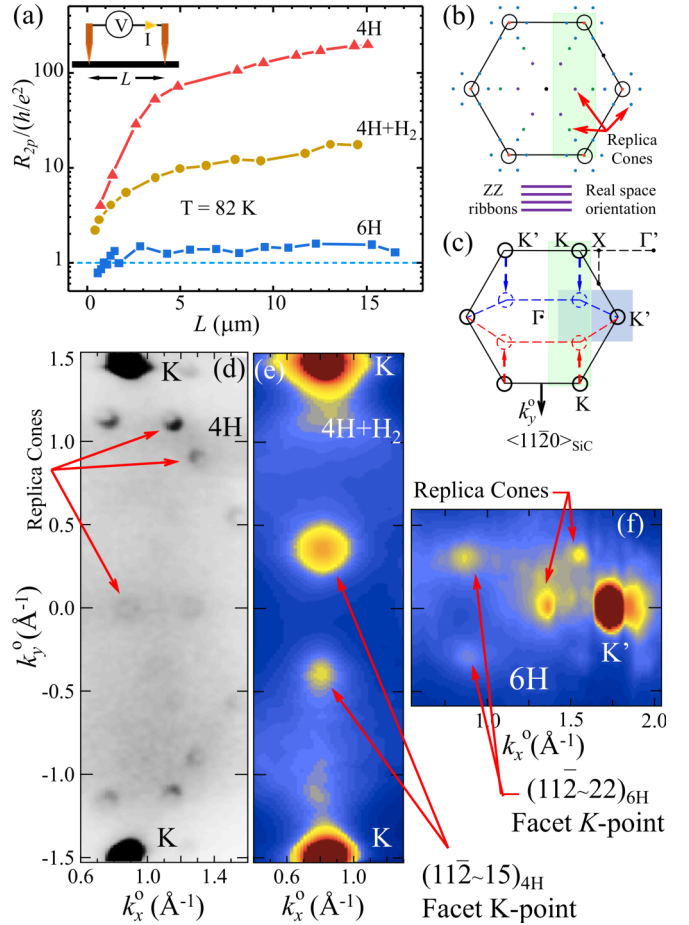


FIG. 2. (a) The 2-point resistance, $R_{2p}$, normalized by $h/e^2$ vs probe separation for three different ZZ ribbons: 4*H*, 4*H*+H-passivated, and 6*H*. (b) and (c) Graphene (0001) BZ. Dots in (b) are ($6 \times 6$) replica cone positions. (c) The compressed graphene BZs (dashed lines and circles) of the {11$\bar{2}$n} (blue) and {$\bar{1}\bar{1}$2n} (red) plotted in the (0001) coordinate frame. Panels (d), (e), and (f) show ARPES constant-$E$ cuts for three ZZ-sidewall samples ($E - E_F = -0.09$ eV and $h\nu = 36$ eV). (d) A cut for 4*H* ZZ ribbons [green area in (b) and (c)] showing intensity from both (0001) and ($6 \times 6$) replica cones. (e) Same as (d) but after H₂ passivation. Intensity from {11$\bar{2} \sim 15$}$_{4H}$ facet Dirac cones becomes visible. (f) A cut for 6*H* ZZ ribbons [blue area in (c)]. The {11$\bar{2} \sim 22$}$_{6H}$ graphene facet cones are marked.

## III. RESULTS

### A. Structure

Figure 2 also compares ARPES intensity cuts, $I(\vec{k}^0, E)$ at fixed binding energy (BE = $E - E_F$), for three different ZZ-ribbon arrays: 4*H*, 4*H*-H₂-passivated, and 6*H* ribbons. $\vec{k}^0$ is in the (0001) surface plane. The facet walls are sufficiently well ordered after graphene growth so that the 40 μm diameter ARPES beam, averaging over ~100 sidewalls, gives a good ensemble average of the ribbon band structure [25]. The ARPES intensity is related to the 2D band dispersion $E(\vec{k}_\parallel)$, where $\vec{k}_\parallel$ is in the plane of the local surface. Because of the ARPES beam size, bands from both the (0001) and the opposing {11$\bar{2}$n} and {$\bar{1}\bar{1}$2n} facets are simultaneously

measured [see Fig. 2(c)]. Any Dirac cones from graphene on the facets appear shifted in $k_y^0$ relative to the cones of the (0001) Brillouin zone (BZ) [see Fig. 2(c)] [25]. When we attempt to grow ZZ ribbons on 4$H$ trenches, the $I(\vec{k}_{\parallel}^0, E)$ map in Fig. 2(d) only shows $K$-point cones and 6th-order replica cones associated with the reconstructed graphene-SiC(0001) surface [see Fig. 2(b)] [14,26]. There is no evidence of rotated Dirac cones from graphene on the facets. Either no graphene has grown or the graphitic carbon that did grow is bonded strongly enough to the SiC facet to significantly distort the graphene's $\pi$ bands [12]. The lack of Dirac cones on 4$H$ sidewalls persists up to temperatures where the SiC steps melt [11]. As we now show, the 4$H$ ZZ-ribbon cones from facet graphene appear once the graphene-SiC bonding is broken.

To demonstrate that graphene is strongly bonded to the 4$H$ sidewalls, we have $H_2$-passivated the 4$H$ ribbons in Fig. 2(d). $H_2$ passivation is known to break the graphene-substrate silicon bonds, turning a semiconducting graphene film on SiC(0001) [13,14] to a metallic film [27]. Figure 2(e) shows the same ARPES map as Fig. 2(d) but after $H_2$ passivation. The passivated sample shows a set of modified Dirac cones appearing along the line between the two $K$ points of the (0001) surface. As shown in the schematic BZ in Fig. 2(c), these cones are from graphene on the tilted facets. We note that the different facet cone intensities are due to ARPES matrix element effects caused by the different angles between the photon polarization vector and the opposing facet normals. The angle between the (0001) plane and the facet normal, $\theta_F$, is found from the $\vec{k}_y^0$ positions of the facet cones and from their asymmetry. The asymmetry is a result of ARPES matrix element effects [28,29] (see Supplemental Material [20] for details). We find $\theta_F = 23.6° \pm 0.5°$, corresponding to $\{11\bar{2} \sim 15\}_{4H}$ planes.

While graphene-Si bonding causes 4$H$ ZZ-sidewall graphene to be nonmetallic, graphene grown on 6$H$-SiC $\{11\bar{2}n\}_{6H}$ facets is naturally metallic. Figure 2(f) shows a partial ARPES map for ZZ ribbons grown on 6$H$-SiC. Unlike 4$H$ ribbons, Dirac cones from 6$H$ facets appear after growth without passivation. The 6$H$ facets have $\theta_F = 24° \pm 0.5°$, corresponding to graphene ribbons on $\{11\bar{2} \sim 22\}_{6H}$ planes.

The fact that the $\pi$ bands are observed without $H_2$ passivation demonstrates that 4$H$ ZZ-sidewall graphene is bonded very differently to the substrate compared to 6$H$ ribbons. We believe that the graphene-substrate interaction on the 4$H$ facet is analogous to the buffer graphene–substrate interaction where the graphene becomes semiconducting because of graphene-Si bonds. Our 4$H$ ZZ-graphene results imply that there are more Si dangling bonds available to interact with the sidewall graphene on 4$H$ compared to 6$H$ facets. More structural work will be required to understand the atomic structure of 4$H$ and 6$H$ facets before this conjecture can be quantified.

While it is clear that the SiC polytype matters for graphene sidewall growth, it was certainly assumed that the two bulk-terminated, nonpolar, 4$H$- and 6$H$-SiC $\{11\bar{2}n\}$ planes would be very similar and lead to similar ZZ-graphene sidewall ribbons. It turns out, however, that their energetics are known



FIG. 3. $F(\theta)$ plots for (a) 4$H$- and (b) 6$H$-SiC based on calculated (black lines) and experimental (dots) growth rates for two temperatures (modified from Ref. [30]). Both 4$H$- and 6$H$-SiC polytypes have pronounced minima for $\{1\bar{1}0n\}$ facets, indicating stable AC steps. In contrast, stable ZZ $\{11\bar{2}n\}$ facets only exists on 6$H$-SiC, the $\{11\bar{2}9\}_{6H}$. Blue dashed lines mark the known stable 4$H$ AC facet after graphene growth (from Refs. [25,31]). Red dashed lines mark the stable ZZ facets from this work. Gray shaded area in (b) was estimated by STM in Ref. [9]. Gray hatched area shows a range of angles where disordered ZZ-sidewall graphene grows in deep trenches [9].

to be very different. Figure 3 shows the surface free energy as a function of angle, $F^{SiC}(\theta)$, for both 4$H$- and 6$H$-SiC (modified from Ref. [30]). The plots include facet angles for AC $\{1\bar{1}0n\}$ and ZZ $\{11\bar{2}n\}$ planes. Minima in $F(\theta)$ usually correspond to stable facets. Since well-defined minima are calculated and measured for AC $\{1\bar{1}0n\}$ planes on both 4$H$- and 6$H$-SiC, there are stable AC facets on both polytypes. In contrast, $F^{SiC}(\theta)$ for ZZ facets in Fig. 3 predicts that only the 6$H$-SiC polytype will have a stable facet: the $\{11\bar{2}9\}_{6H}$ at $\theta_F = 47.5°$. Clearly the polytype matters in the facet stability of 4$H$ and 6$H$ AC and ZZ facet walls.

Of course we do not expect $F^{SiC}(\theta)$ for bare SiC to be the same as $F^{G+SiC}(\theta)$ when the facets have graphene on them. There are apparent differences in $F(\theta)$ after graphene growth. Experimental high-resolution transmission electron microscopy (HRTEM) measurements [31] and ARPES [25] on graphene growth on 4$H$-SiC sidewalls find that the (1$\bar{1}$07), not the (1$\bar{1}$05), is the dominant observed facet. Figure 3 simply shows that it is not unreasonable that there can be differences in ZZ-sidewall graphene grown on the two polytypes. In this work, the stable facet walls when ZZ-sidewall graphene grows are 23.6° and 24° for 4$H$- and 6$H$-SiC, respectively. From an energetics point of view, however, the 6$H$ $\{11\bar{2} \sim 22\}_{6H}$ planes must have a lower free energy than

FIG. 4. (a) Post-graphene-growth profile near the bottom of a 25-nm-high 6H ZZ-edge step. (b) A $dI/dV$ image of the step in (a). (c) Histogram of 250 facet widths plotted by both relative frequency and areal coverage. (d) $dI/dV$ image comparison of the macroscopic (0001) surface and an adjacent nano (0001) terrace separated by a ZZ-edge step. (e) Bonding geometry of a ZZ-edge ribbon to a commensurate bulk-terminated $(6\sqrt{3} \times 6\sqrt{3})R30°$ SiC surface. (f) Atomic resolution image of a facet-(0001) boundary showing the chiral meandering (dashed line) of graphene at the step edge.

the 4H $\{11\bar{2} \sim 15\}$ counterparts because the 4H-SiC surface prefers to bond to graphene to lower its energy.

Unlike AC steps where a single $(1\bar{1}07)$ facet covers $\sim$70% of the step area [31], 6H ZZ steps have a complicated facet structure [9,18]. The ZZ steps consist of many $\{11\bar{2} \sim 22\}_{6H}$-(0001) plane pairs [see Figs. 4(a)]. The $\{11\bar{2} \sim 22\}_{6H}$ facets have a broad width distribution as shown in Fig. 4(c). The histogram gives an average 6H facet width of $\bar{w}_f \sim 6 \pm 8$ nm with a high number of 1–2 nm facets. The important question is how the graphene ribbon width distribution, $N(W_r)$, is related to the facet width distribution $N(w_f)$; i.e., does the facet graphene flow onto and over the (0001) nanoterraces as a continuous very wide ribbon (like a carpet draping over a staircase), or does the facet graphene terminate somewhere on an adjacent (0001) terraces so that $N(W_r) \sim N(w_f)$? As we will show, both STM and ARPES find that the graphene ribbon width is similar to the facet width.

Figure 4(b) shows a $dI/dV$ map of the step profile in Fig. 4(a). The fact that the facets are bright compared to the (0001) nanoterraces indicates that there is a discontinuity in the electronic structure of the graphene on facet and semiconducting graphene that is known to grow on the nanoterraces [31]. These results suggest that the facet graphene either terminates into the SiC(0001) surface or transitions into a semiconducting form of graphene on the (0001) nanosurface. In either case, the results suggest that graphene is a metallic ribbon of width proportional to the facet width. As we will show below, this statement is supported by the ARPES data.

## B. Electronic structure

Both the 6H- and 4H-passivated ZZ ribbons are sufficiently ordered to allow detailed area-averaged band measurement. Figure 5(a) shows the 6H ribbon's band intensity for $k_x^f$ along the $K'K\Gamma'$ direction of the $(11\bar{2} \sim 22)$ facet plane. The 6H ZZ ribbon's $\pi^-$ and $\pi^+$ bands' momentum and widths were determined from Lorentzian fits to momentum distribution curves (MDCs): $I(k_x^f, \mathrm{BE})$ at fixed BE (see Supplemental Material [20]). In this paper, we will refer to integrated $\pi$-band intensity as the integrated Lorentzian intensity from these fits. The $\pi$-band positions (marked by circles) show a distorted Dirac cone. For BE $< -0.4$ eV, the bands have an asymmetric dispersion with a larger band velocity, $v_F$, for the $\pi^+$ band ($v_F^+/v_F^- \sim 1.7$). Both tight-binding (TB) and *ab initio* models predict this asymmetry for narrow ribbons [32,33].

For BE $> -0.4$ eV, the MDC fits show a consistent apparent splitting of $\pi$ bands [see Figs. 5(a) and 5(b)]. While the splitting appears unusual, it is a result of a distribution of the valence band maximum $(\mathrm{VB_m})$ positions $(k_x^m)$ from a ribbon width distribution on the facets that contain a large number of sub-5-nm parallel ribbons. To demonstrate this, we use a TB model for the ribbon's band structure. In this model the $n = 0$ subband is due to the ribbon edges (the edge state). The $k_y^f$ wave vector for this state is imaginary, localizing the wave function to the edges for $k_c \leqslant k_x^f \leqslant \mathrm{X}$, where the critical momentum $k_c$ depends on ribbon width, $W_r$ [33]:

$$k_c = \frac{2}{a} \arccos\left(\frac{1}{2}\frac{W}{W+d}\right); \tag{1}$$

$d$ is the spacing between ZZ chains (see Fig. 2). In both TB and first-principles models, the top of the $n = 1$ subband corresponds to the ribbon's $\mathrm{VB_m}$ [32]. To a very good approximation, $\mathrm{VB_m}$ occurs at $k_x^m \sim k_c$ (see Supplemental Material). For ribbons with $W \gg d$, $\mathrm{VB_m}$ occurs at the $K$ point. Ribbons with $W \sim d$ have $\mathrm{VB_m}$ shifted to higher $k_x$. Figure 5(b) compares the calculated $k_c$ position from Eq. (1) using the experimental $N(w_f)$ distribution in Fig. 4(c). We have convoluted the calculated $k_x$ with a $\Delta k_x = 0.05$ Å$^{-1}$ window consistent with the measured Lorentzian width. The calculated $\mathrm{VB_m}$ distribution reproduces the asymmetric ARPES intensity very well. This can only happen if $N(W_r) \sim N(w_f)$, i.e., $W_r \sim w_f$.

The equality of the facet and graphene ribbon widths also explains the VB's intensity decay and the $\pi$ bands' momentum broadening for BE $> -0.4$ eV. To show this, we use the calculated $n = 0$ subband energy splitting, $\Delta^0(W_r)$, at the $K$ point in the $GW$ approximation [32]:

$$\Delta^0 \approx A/(W_r + \delta), \tag{2}$$

where $A = 38$ eV Å and $\delta = 16$ Å [32]. Roughly, $\mathrm{VB_m}$ is $\sim 0.5\Delta^0$ below $E_F$ for neutral ribbons. Using the STM-measured $w_f$ distribution for $N(W_r)$ in Eq. (2) gives the average position of the valence band to be $\mathrm{VB_m} = 0.44$ eV with a distribution of $\Delta\mathrm{VB_m} = 0.24$ eV. These values are marked on the plot of the 6H ZZ ribbon $\pi$-band intensity, $I(\mathrm{BE})$, in Fig. 5(c). They are in good agreement with experimental intensity that has a broad decay centered around an inflection point near BE $= -0.5$ eV.
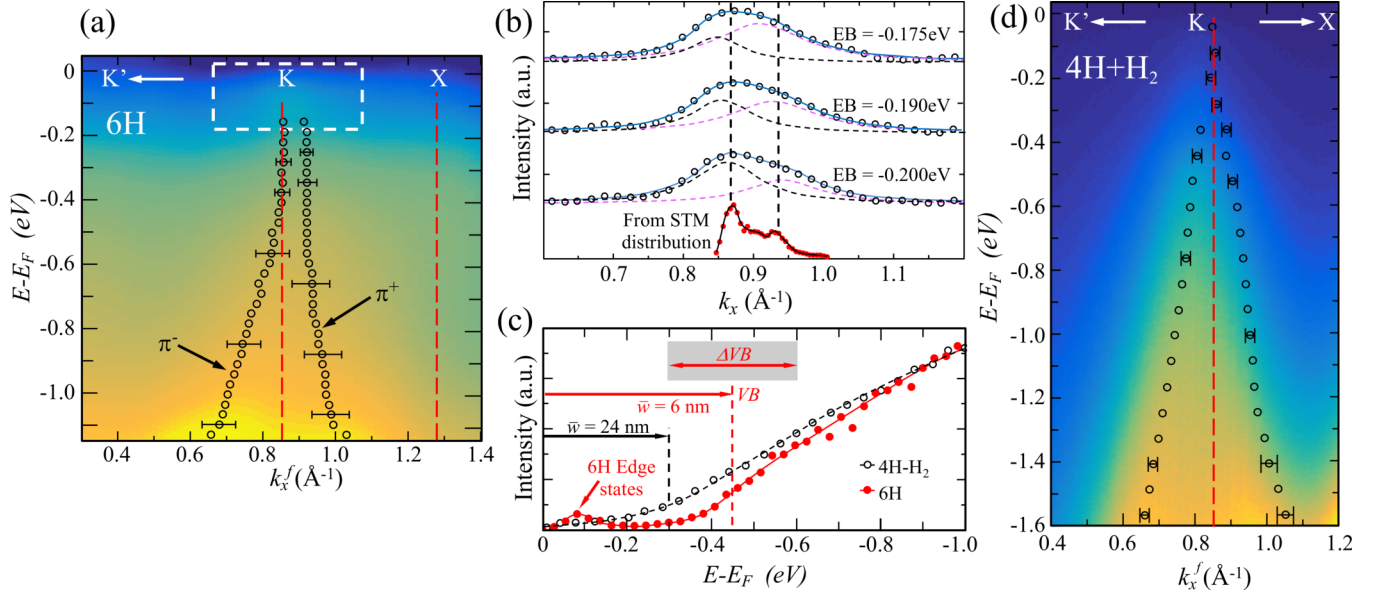
FIG. 5. (a) ARPES-measured bands of *6H* ZZ-sidewall ribbons along the $K'K\Gamma'$ direction (parallel to the ZZ edge). $T_{\text{sample}} = 100$ K. $k_x^f$ is in the plane of the $(11\bar{2} \sim 22)$ facet. Circles (○) mark the band positions. (b) Typical MDC fits showing the $\pi$-band asymmetry for BE $> -0.4$ eV. Solid red circles show the predicted asymmetry from the measured facet $N(w_f)$ distribution and Eq. (1). (c) Integrated $\pi$-band intensity for *6H* (red circles) and $H_2$-passivated *4H* ribbons (black circles). Red arrows mark the estimated valence band edge and width from *6H* STM ribbon $N(w_f)$. (d) ARPES bands from $H_2$-passivated *4H* ZZ ribbons along the $K'KX$ direction (30 nm steps). $k_x^f$ is in the $(11\bar{2} \sim 15)_{4H}$ plane.

Finally, the $\pi$-band $\Delta k_x^f$ broadening near the inflection point of the integrated *6H* $\pi$-band intensity [BE $\sim -0.45$ eV in Fig. 5(c)] is $\sim 0.17$ Å$^{-1}$, three times the broadening for BE closer to $E_F$. The larger $\Delta k_x^f$ near VB$_m$ is caused by overlapping subband energies from ribbons with different widths. Again, area-averaged ARPES contains intensity from a distribution of subbands, $n(W_r)$ (shifted up and down in BE), that leads to an apparent $\Delta k_x$ broadening of the $\pi$ bands. To estimate $\Delta k_x$, we assume a linear $\pi$-band dispersion, $E = \hbar \tilde{c} k$, where $\tilde{c}$ is the average measured band velocity of the $\pi$ bands. If the apparent band broadening is $\Delta E \approx \delta \Delta^0(W_r)$, then $\Delta k_x^f$ is given by

$$\Delta k_x^f \approx \frac{\Delta^0(\bar{w}_f)\Delta \bar{w}_f}{\hbar \tilde{c}(\bar{w}_f + \delta)}, \tag{3}$$

where we have again assumed that $w_f = W_r$. Using the measured STM values for $\bar{w}_f$ gives $\Delta k_x^f = 0.14$ Å$^{-1}$, in good agreement with the measure value. In short, the $\pi$ band's shape, splitting, and $\Delta k_x^f$ broadening are all consistent with *4H* ZZ ribbons having a width approximately equal to the $(11\bar{2} \sim 22)$ facet widths.

What distinguishes ZZ ribbons from AC ribbons is the existence of a ZZ-edge state [33]. Because these states are localized near the ribbon edges, their spectral weight is low. Nevertheless, we find two states, $\epsilon_1$ and $\epsilon_2$, near $E_F$ in Fig. 5(a) that we can identify as edge states. The states are seen more clearly in Figs. 6(a) and 6(b). The energy distribution curves (EDCs), $I(\text{BE}, k_x^f)$ at fixed $k_x^f$, show that the states are essentially dispersionless along $KK'\Gamma'$ [see Fig. 6(a)]. EDCs near $K$ in Fig. 6(b) show that the BEs of the two states are $\epsilon_1 = -56$ and $\epsilon_2 = -103$ meV. Their energy width is 58 meV, essen-

tially the expected thermal broadening for the $T = 100$ K sample. We identify these bands as ZZ-edge states associated
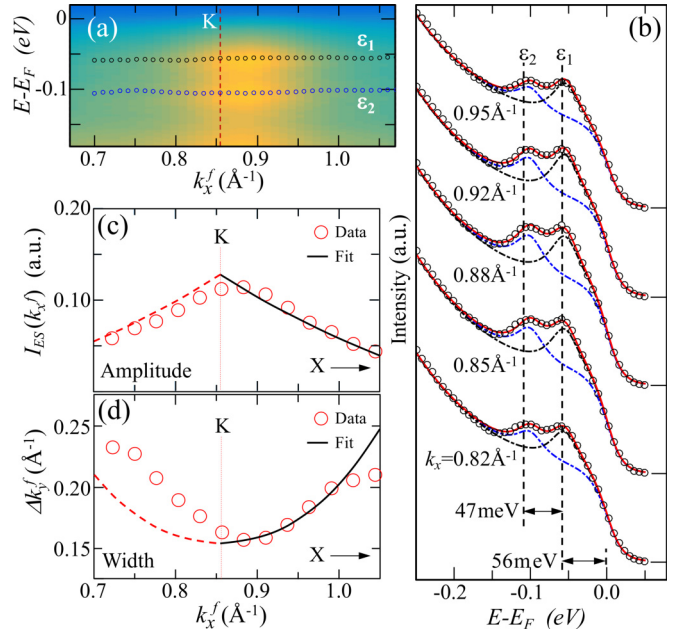


FIG. 6. (a) Close-up of *6H* ZZ-sidewall ribbon band structure near $E_F$ [dashed box in Fig. 5(a)] showing flat bands, $\epsilon_1$ and $\epsilon_2$. Circles ○ mark the peak positions from EDC fits. (b) Sample EDCs near $E_F$ in (a) (○ are data). A two-Lorentzian (dashed black and blue lines) plus background and Fermi-Dirac cutoff fit is shown (red solid line). Panels (c) and (d) show $\epsilon_1$ and $\epsilon_2$ average intensity and $\Delta k_y^f$ width, respectively, vs $k_x^f$. Solid and dashed lines are TB estimates described in the text.

with asymmetric edge terminations. This assignment follows from three observations: (i) Their intensity and perpendicular broadening along $K < k_y^f < X$ is consistent with predictions, (ii) the states do not disperse in either $k_x^f$ or $k_y^f$, and (iii) the bands are narrow in $E$.

Figures 6(c) and 6(d) show that the average $\epsilon_1$ and $\epsilon_2$ intensities decrease for $k_x^f > K$ while their perpendicular bandwidths, $\Delta k_y^f$, increase $k_x^f > K$. These are the expected trends for edge states in a TB model for ZZ ribbons. Using symmetric ZZ edges, the TB edge state's charge density, $\rho(y)$, is completely localized at the edge when $k_x^f = \pi/a$ (the 1D $X$ point). At lower $k_x^f$, it become more delocalized until at the $K$ point ($k_x^f = 2\pi/3a$) $\rho(y)$ is uniform perpendicular to the edge [33]. Therefore, the edge-state bandwidth, $\Delta k_y^f \sim 2\pi/\Delta y$, is largest at $X$ and smallest at $K$. Furthermore the edge-state intensity, $I_{ES}(k_x^f)$, is proportional to $\cos(k_x^f a/2)$ [33]. Thus $I_{ES}(k_x^f)$ is a maximum at $K$ and decreases as $k_x^f$ approaches the $X$ point. The TB estimates (see Supplemental Material [20]) for $I_{ES}(k_x^f)$ and $\Delta k_y^f$ are plotted in Figs. 6(c) and 6(d). Note that $\Delta k_y^f$ has been convoluted with a 0.16 Å window to match the experimental minimum at $K$. The dashed lines in Figs. 6(c) and 6(d) are mirrored versions of the solids lines about $K$.

While there are similarities between the 6$H$ ribbon edge states and TB predictions, there are significant differences. First, the measured edge states are narrow in energy ($\Delta E = 58$ meV). Since the edge-state splitting, $\Delta^0$, from symmetrically terminated ribbons depends on $W_r$, we would expect $\epsilon_1$ and $\epsilon_2$ to have a significant $\Delta E$ due to $N(W_r)$. From Eq. (2), the STM $w$ distribution would give $\Delta E \sim 0.5$ eV, nine times larger than measured. Furthermore, the $\epsilon_1$ and $\epsilon_2$ bands are flat while theoretical models for symmetric edge terminations predict a strong dispersion along the $K'KX$ direction, regardless of whether or not they are antiferromagnetically (AF) or ferromagnetically (F) coupled [32,34–37]. Asymmetric-termination models, on the other hand, give rise to nearly flat bands near $E_F$ [17,38]. In particular, $sp^2$ termination on one edge and $sp^3$ on the other give rise to nearly flat bands through the entire 1D BZ whose energies are essentially independent of the ribbon width [17]. In other words, our edge states are not from symmetric ribbons.

The fact that the ARPES data point to asymmetric edges is not unexpected. Based on HRTEM images of 4$H$-SiC AC steps, the ribbons terminate into semiconducting buffer graphene on the macroscopic (0001) surface through $sp^2$ C-C bonds [31]. At the step bottom, the ribbon terminates by either C-Si $sp^3$ bonds to the substrate SiC [type I termination in Fig. 7(a)] or by an intermediate $sp^2$ C-C bond to buffer graphene on (0001) nanofacets [type II in Fig. 7(b)]. The asymmetric type I termination is more complicated than Fig. 7 indicates. While the ribbon-buffer edge is commensurate and ordered, the C-Si $sp^3$ edge is incommensurate with the SiC [see Figs. 4(e)] [16]. The aperiodic C-Si $sp^3$ bonding leads to >60% bond defects with the edge-carbon either unbonded or rehybridized in some complicated way. This fraction can be larger since the actual (0001) surface has 20% less Si than a bulk-terminated surface [39,40]. The edge structure is also complicated by the patterned step edges being slightly rotated with respect to the SiC, $\phi \sim 2°$–2.5°. This leads to a chirality in the step edges as the graphene terminates into
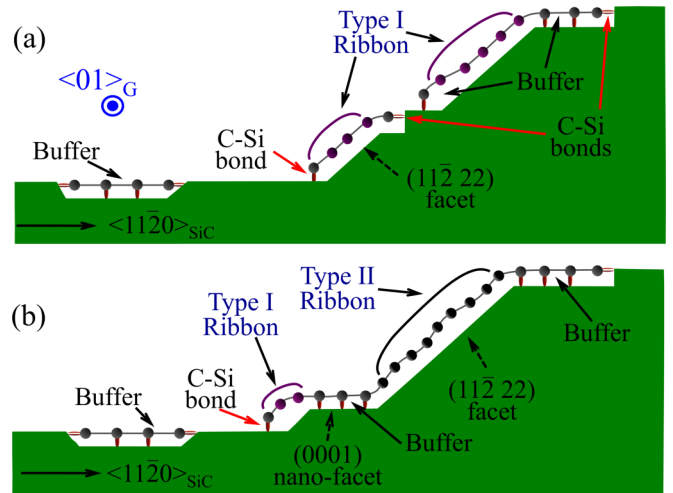


FIG. 7. Two edge-terminated 6$H$ ZZ ribbons. Functionalized (buffer) graphene is represented by gray circles bonded to the SiC. (a) Type I ribbons terminated by C-C bonds into buffer graphene on one side and C-Si bonds to the substrate on the other side. (b) A type II termination with metallic graphene terminated on both sides by C-C bonds into buffer graphene.

the (0001) planes [see Fig. 4(f)]. Line defects in graphene are also known to lead to flatter bands over the entire zone compared to H-terminated ribbons [41]. Regardless of the details of the asymmetric C-Si $sp^3$ edges, the narrow energy widths and dispersionless character of the observed $\epsilon_1$ and $\epsilon_2$ bands are consistent with edge states from asymmetric edge terminations in the sidewall SiC system.

While type II ribbons resemble a waveguide geometry with metallic graphene ribbons bonded to a semiconducting graphene on both edges, their terminations are also asymmetric. This is because buffer graphene on macroscopic (0001) and nano (0001) terraces are structurally and electronically different. Only the macroscopic (0001) surface shows the typical (6 × 6) reconstruction [see Fig. 4(d)] [42]. Furthermore, $dI/dV$ data clearly show a bias-dependent contrast difference between macroscopic and nano (0001) surfaces (see Supplemental Material [20]). How this waveguide affects transport is an open question. Regardless, the type II ribbon can be thought of as an asymmetric type I ribbon with a more complicated structure between $sp^2$ and $sp^3$ edges.

Data on 4$H$ H$_2$-passivated ribbons imply a very different ribbon geometry compared to 6$H$ ribbons. Figure 5(d) shows the band structure from the passivated 4$H$ ZZ ribbons. The cut through the BZ is the same cut as in Fig. 5(a). The flat edge-state bands below $E_F$ are not seen in the passivated 4$H$ sample. We would expect a change in the edge states because the hydrogen treatment would not only transform semiconducting buffer graphene to metallic on all (0001) terraces [43]; it would also break any C-Si bonds at the type I edges and hydrogenate a large fraction of unbonded carbon along the edges. While H$_2$ passivation can $p$-dope graphene by ~100 meV and shift the states above $E_F$ where they would not be visible in ARPES [27], the diffusive conductance measured in transport [see Fig. 2(a)] suggests either that there are no edge states or that any finite-size gap is too small to electronically isolate a particular subband.

Besides the missing edge states, there are other differences in the 4$H$-passivated $\pi$ bands compared to 6$H$ ribbons. Unlike 6$H$ ribbons, the $H_2$-passivated 4$H$ ribbon's $\pi^-$ and $\pi^+$ bands are nearly symmetric about the $K$ point with the same band velocity found in macroscopic sheets, $v_F \sim 1 \times 10^6$ m/sec. The $k_x^f$ position of VB$_m$ is essentially at the $K$ point and there is no evidence of a $\Delta k_x^f$ splitting of the $\pi$ bands. This rules out any significant number of sub-5-nm ribbons. If a VB$_m$ exists, it must occur at BE $\gtrsim -0.3$ eV. According to Eq. (2), that BE would imply a 4$H$-ribbon width of $\bar{W}_{4H} > 24$ nm. It is clear that either the 4$H$ step is approximately a single (11$\bar{2} \sim 15$) facet or the sidewall graphene that grows is only terminated at the top and bottom of the step.

## IV. CONCLUSIONS

To summarize, we demonstrate that metallic ZZ-edge epitaxial graphene ribbons only grow on the $\{11\bar{2}, 22\}_{6H}$ facets of the 6$H$-SiC polytype. While graphene does grow on the 4$H$ polytype, it is bonded to the facet walls in a way that heavily modifies the graphene $\pi$ bands, similarly to why the first graphene layer on SiC(0001) is semiconducting because of graphene-SiC bonds. The nonmetallic 4$H$ ribbons can be turned metallic by $H_2$ passivation that breaks the graphene-sidewall bonds.

STM, STS, and ARPES measurements show that 6$H$ facet walls consist of multiple $\{11\bar{2}, 22\}_{6H}$-(0001) nanoplane pairs. These pairs appear electronically isolated from each other and give rise to a width distribution where more than $> 80\%$ of the ribbons are less than 12 nm wide ($>50\%$ between 1–3 nm). ARPES measurements find two nondispersing states 56 and 103 meV below $E_F$ that are identified as ZZ-ribbon edge states. These states' dispersion, width, and intensity

dependencies on in-plane momentum indicate that they originate from asymmetrically terminated ZZ edges. The lack of an observed crossing of the two states suggests that they are antiferromagnetically aligned on opposite edges of the ribbon. Transport measurements show that these 6$H$ ZZ ribbons are ballistic conductors up to at least 16 $\mu$m.

ARPES shows that unlike 6$H$ sidewall ribbons, the 4$H$ sidewall ribbons appear to be a single wide sheet over the entire 4$H$ facet. Both the passivated and unpassivated 4$H$ sidewall ribbons show no evidence of $n$-doped edge states. Two-point transport measures for both the 4$H$ and $H_2$-passivated 4$H$ sidewall ribbons indicate that they are diffusive conductors. It is possible that nonlocal probe measurements on 4$H$ ribbons may demonstrate ballistic transport even though there is no metallic graphene on the facets. It is known that narrow metallic graphene ribbons form on the (0001) surface near the facet step edge [12]. Conduction through these ribbons cannot be discriminated against using nonlocal gates. Also, graphene grown on shallow trenches, less than 5 nm deep, may interact differently with the SiC facet because of the ribbons' finite radius of curvature, preventing bonding to the facet and allowing them to remain metallic. These two possibilities remain to be systematically tested.

[1] C. Berger, Z. Song, T. Li, X. Li, A. Y. Ogbazghi, R. Feng, Z. Dai, A. N. Marchenkov, E. H. Conrad, P. N. First, and W. A. de Heer, J. Phys. Chem. B **108**, 19912 (2004).

[2] K. Nakada, M. Fujita, G. Dresselhaus, and M. S. Dresselhaus, Phys. Rev. B **54**, 17954 (1996).

[3] M. Sprinkle, M. Ruan, Y. Hu, J. Hankinson, M. Rubio-Roy, B. Zhang, X. Wu, C. Berger, and W. A. de Heer, Nat. Nanotechnol. **5**, 727 (2010).

[4] K. Todd, H.-T. Chou, S. Amasha, and D. Goldhaber-Gordon, Nano Lett. **9**, 416 (2009).

[5] K. A. Ritter and J. W. Lyding, Nat. Mater. **8**, 235 (2009).

[6] M. Y. Han, J. C. Brant, and P. Kim, Phys. Rev. Lett. **104**, 056801 (2010).

[7] E. R. Mucciolo, A. H. Castro Neto, and C. H. Lewenkopf, Phys. Rev. B **79**, 075407 (2009).

[8] F. Sols, F. Guinea, and A. H. Castro Neto, Phys. Rev. Lett. **99**, 166803 (2007).

[9] J. Baringhaus, F. Edler, and C. Tegenkamp, J. Phys.: Condens. Matter **25**, 392001 (2013).

[10] J. Baringhaus, M. Ruan, F. Edler, A. Tejeda, M. Sicot, I. Taleb, A.-P. Li, Z. Jiang, E. H. Conrad, C. Berger, C. Tegenkamp, and W. A. de Heer, Nature (London) **506**, 349 (2014).

[11] M. S. Nevius, Improved growth, ordering, and characterization of sidewall epitaxial graphene nanoribbons, Ph.D. thesis, Georgia Institute of Technology, 2016.

[12] M. S. Nevius, F. Wang, C. Mathieu, N. Barrett, A. Sala, T. O. Mente, A. Locatelli, and E. H. Conrad, Nano Lett. **14**, 6080 (2014).

[13] K. V. Emtsev, F. Speck, T. Seyller, L. Ley, and J. D. Riley, Phys. Rev. B **77**, 155303 (2008).

[14] M. S. Nevius, M. Conrad, F. Wang, A. Celis, M. N. Nair, A. Taleb-Ibrahimi, A. Tejeda, and E. H. Conrad, Phys. Rev. Lett. **115**, 136802 (2015).

[15] M. N. Nair, I. Palacio, A. Celis, A. Zobelli, A. Gloter, S. Kubsky, J.-P. Turmaud, M. Conrad, C. Berger, W. de Heer, E. H. Conrad, A. Taleb-Ibrahimi, and A. Tejeda, Nano Lett. **17**, 2681 (2017).

[16] M. Conrad, F. Wang, M. Nevius, K. Jinkins, A. Celis, M. Narayanan Nair, A. Taleb-Ibrahimi, A. Tejeda, Y. Garreau, A. Vlad, A. Coati, P. F. Miceli, and E. H. Conrad, Nano Lett. **17**, 341 (2017).

[17] X. Deng, Z. Zhang, G. Tang, Z. Fan, and C. Yang, Carbon **66**, 646 (2014).

[18] J. Aprojanz, S. R. Power, P. Bampoulis, S. Roche, A.-P. Jauho, H. J. W. Zandvliet, A. A. Zakharov, and C. Tegenkamp, Nat. Commun. **9**, 4426 (2018).

[19] C.-Y. Lu, J. A. Cooper, T. Tsuji, G. Chung, J. R. Williams, K. McDonald, and L. C. Feldman, IEEE Trans. Electron Devices **50**, 1582 (2003).

[20] See Supplemental Material at http://link.aps.org/supplemental/10.1103/PhysRevB.100.045425 for details on ribbon growth procedures alone with experimental details of ARPES, STM and transport techniques. The supplement also discusses how the step facet angles are uniquely determined from ARPES along with fitting methods for ARPES MDCs and EDCs. The supplement also describes how TB and ab-initio ribbon band structure predictions are used to estimate the ribbon's VB maximum, VB width along with predictions for the edge state's intensity and $kx$ width.

[21] W. A. de Heer, C. Berger, M. Ruan, M. Sprinkle, X. Li, Y. Hu, B. Zhang, J. Hankinson, and E. Conrad, Proc. Natl. Acad. Sci. USA **108**, 16900 (2011).

[22] C. Didiot, A. Tejeda, Y. Fagot-Revurat, V. Repain, B. Kierren, S. Rousset, and D. Malterre, Phys. Rev. B **76**, 081404(R) (2007).

[23] T.-H. Kim, Z. Wang, J. F. Wendelken, H. H. Weitering, W. Li, and A.-P. Li, Rev. Sci. Instrum. **78**, 123701 (2007).

[24] A.-P. Li, K. W. Clark, X.-G. Zhang, and A. P. Baddorf, Adv. Funct. Mater. **23**, 2509 (2013).

[25] J. Hicks, A. Tejeda, A. Taleb-Ibrahimi, M. S. Nevius, F. Wang, K. Shepperd, J. Palmer, F. Bertran, P. Le Fevre, J. Kunc, W. A. de Heer, C. Berger, and E. H. Conrad, Nat. Phys. **9**, 49 (2013).

[26] A. Bostwick, T. Ohta, T. Seyller, K. Horn, and E. Rotenberg, Nat. Phys. **3**, 36 (2007).

[27] C. Riedl, C. Coletti, T. Iwasaki, A. A. Zakharov, and U. Starke, Phys. Rev. Lett. **103**, 246804 (2009).

[28] E. L. Shirley, L. J. Terminello, A. Santoni, and F. J. Himpsel, Phys. Rev. B **51**, 13614 (1995).

[29] A. Bostwick, T. Ohta, J. L. McChesney, K. V. Emtsev, T. Seyller, K. Horn, and E. Rotenberg, New J. Phys. **9**, 385 (2007).

[30] N. Nordell, S. Karlsson, and A. Konstantinov, Mater. Sci. Eng. B **61-62**, 130 (1999).

[31] I. Palacio, A. Celis, M. N. Nair, A. Gloter, A. Zobelli, M. Sicot, D. Malterre, M. S. Nevius, W. A. de Heer, C. Berger, E. H. Conrad, A. Taleb-Ibrahimi, and A. Tejeda, Nano Lett. **15**, 182 (2015).

[32] L. Yang, C.-H. Park, Y.-W. Son, M. L. Cohen, and S. G. Louie, Phys. Rev. Lett. **99**, 186801 (2007).

[33] K. Wakabayashi, K.-i. Sasaki, T. Nakanishi, and T. Enoki, Sci. Technol. Adv. Mater. **11**, 54504 (2010).

[34] Y.-W. Son, M. L. Cohen, and S. G. Louie, Phys. Rev. Lett. **97**, 216803 (2006).

[35] L. Pisani, J. A. Chan, B. Montanari, and N. M. Harrison, Phys. Rev. B **75**, 064418 (2007).

[36] J. Jung and A. H. MacDonald, Phys. Rev. B **79**, 235433 (2009).

[37] O. V. Yazyev, Rep. Prog. Phys. **73**, 056501 (2010).

[38] G. Lee and K. Cho, Phys. Rev. B **79**, 165440 (2009).

[39] J. D. Emery, B. Detlefs, H. J. Karmel, L. O. Nyakiti, D. K. Gaskill, M. C. Hersam, J. Zegenhagen, and M. J. Bedzyk, Phys. Rev. Lett. **111**, 215501 (2013).

[40] M. Conrad, J. Rault, Y. Utsumi, Y. Garreau, A. Vlad, A. Coati, J.-P. Rueff, P. F. Miceli, and E. H. Conrad, Phys. Rev. B **96**, 195304 (2017).

[41] S. Dutta and K. Wakabayashi, Sci. Rep. **5**, 11744 (2015).

[42] C. Riedl, U. Starke, J. Bernhardt, M. Franke, and K. Heinz, Phys. Rev. B **76**, 245406 (2007).

[43] J. Sforzini, L. Nemec, T. Denig, B. Stadtmüller, T.-L. Lee, C. Kumpf, S. Soubatch, U. Starke, P. Rinke, V. Blum, F. C. Bocquet, and F. S. Tautz, Phys. Rev. Lett. **114**, 106804 (2015).